J Adv Ceram

Research Article

Interlayer bonding in vat photopolymerization additive manufactured ceramics with enhanced mechanical properties

Keqiang Zhang[1,2,✉], Qiaoyu Meng[2], Zhaoliang Qu[2], Rujie He[2,✉]

Cite this article: Zhang K, Meng Q, Qu Z, et al. *J Adv Ceram* 2026, **15**(5): 9221290. https://doi.org/10.26599/JAC.2026.9221290

ABSTRACT: The performance of vat photopolymerization (VPP) additive manufactured ceramics is critically limited by weak interlayer bonding, which represents a challenge inherent to the layer-by-layer process. However, current research often optimizes stereolithography and sintering as separate stages, overlooking the dynamic evolution of the interlayer. This study introduces a novel paradigm by conceptualizing the interlayer as a dynamic system evolving under photothermal fields. A strategy of cross-process synergistic control, actively interlayer evolution rather than passively reducing defects, was proposed. We systematically investigate key stereolithographic parameters (irradiance, exposure time, and slicing thickness) and sintering protocols, focusing on the collaborative mechanism between photopolymerization dynamics and sintering kinetics in the interlayer. Orthogonal design identifies slicing thickness as the most critical factor. By precisely controlling the ultraviolet (UV) energy input, a controlled incompletely polymerized state is introduced to enhance interlayer bonding via an effective dynamic balance between primary and secondary photopolymerization. Subsequent sintering is tailored to improve the particle packing density at the interlayer. The ZrO_2 ceramic achieves a high flexural strength of 425.89±16.01 MPa and a relative density of 97.21%±0.14% after sintering at 1550 °C for 2 h. This work establishes a framework that links process parameters to interlayer evolution and properties, offering both a practical pathway and a novel theoretical perspective for manufacturing high-performance ceramics.

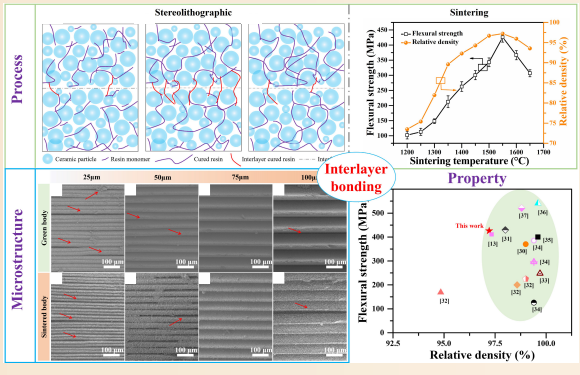

KEYWORDS: interlayer bonding; ZrO_2 ceramic; vat photopolymerization; additive manufacturing; mechanical property

1 Introduction

Additive manufacturing (AM) builds objects layer-by-layer from digital three-dimensional (3D) models, providing exceptional design flexibility, mass customization, and the ability to produce complex, topologically optimized structures that are unattainable through conventional methods [1–3]. Among the AM technologies for ceramics, vat photopolymerization (VPP), particularly stereolithographic (SLA) and digital light processing (DLP), has garnered significant attention owing to its high manufacturing resolution, excellent surface quality, and relatively fast build speeds [4–7]. The VPP process utilizes a photosensitive suspension containing a high solid loading of ceramic particles. A light source, either a laser spot or a projected image, selectively cures the suspension layer-by-layer to form a green body, which is subsequently debinded and sintered to yield a ceramic component [8,9].

Despite these advantages, transitioning from conventional to AM of high-performance ceramic presents substantial scientific and technological challenges. The mechanical properties of VPP fabricated ceramics are lower than those of conventional ceramics and are critically dependent on the elimination of processing defects, which can originate from multiple processes [10]. Recent research has significantly advanced our understanding of VPP processes. Some studies have first focused on developing stable and high solid-loading ZrO_2 ceramic suspensions with suitable rheological and curing properties and examining the effect of these factors on the final mechanical properties of the ceramics [11,12]. Jang *et al.* [13] investigated the effect of solid loading of suspensions on the microstructure and physical properties of ZrO_2 ceramics produced by VPP. They found that defects appeared and the light scattering increased as the solid loading of the ZrO_2 suspension increased. Sun *et al.* [14] investigated the dispersion and rheological behavior of a ZrO_2 suspension through rheometry and ultraviolet–visible (UV–Vis) spectroscopy. Their findings indicated that optimizing the dispersant concentration yields significant benefits.

In addition to ceramic suspension fabrication, the mechanical

[1] College of Materials Science and Engineering, Nanjing Tech University, Nanjing 211816, China. [2] Institute of Advanced Structure Technology, Beijing Institute of Technology, Beijing 100081, China.

✉ Corresponding authors. E-mail: K. Zhang, zhangkeq@126.com; R. He, herujie@bit.edu.cn

Received: January 12, 2026; Revised: February 25, 2026; Accepted: March 24, 2026

properties and densification of the ceramic are critically dependent on a multistage process chain, in which the stereolithographic parameters and the subsequent sintering schedule play a decisive role. The layer-by-layer approach of AM results in anisotropy and weak interlayer bonding that are absent in isotropic bodies fabricated through conventional methods. The "interlayer", an inherent feature, serves as a potential flaw zone that can propagate during the sintering processes, ultimately compromising the density and mechanical integrity of the ceramic component. Inadequate or excessive polymerization can lead to the formation of interlayer defects, which become failure origins after the sintering process [15–17]. Reddy *et al.* [18] addressed the effect of DLP print parameters on the density of green parts and concluded that the density of the ZrO_2 ceramic green and sintered body in the interlayer zone is lower than that of the inlayer zone. Furthermore, ceramic green bodies contain approximately 50% non-ceramic components, leaving numerous pores after the debinding process, particularly the interlayer effects, which pose significant challenges for their sintering process [19,20]. Zhao *et al.* [21] combined AM, pressureless two-step sintering, and hot isostatic pressing (HIP) and successfully produced dense ultrafine-grained Ce–TZP ceramics. However, at present, the stereolithographic process and the high-temperature sintering process are treated as sequential, independent modules for parameter optimization. This stepwise approach fundamentally isolates the analysis of photopolymerization dynamics from sintering kinetics, leading to an incomplete understanding of defect formation and evolution, especially within the interlayer zone. These interlayer zones represent unique microstructural and compositional interfaces formed between successively cured layers. Their properties are not static but are dynamically governed by the initial photopolymerization state of the green body and subsequently transformed during high-temperature thermal treatment.

The fundamental challenge resides not only in the individual imperfections of each process step but also in a critical knowledge gap: the unclear evolution mechanism of this interlayer zone under the continuous influence of photothermal fields at various stages. Traditional stepwise optimization does not adequately account for the dynamic and interconnected characteristics of the interlayer zone. This zone undergoes a transformative process, transitioning from a liquid-suspension interface during printing to a consolidated, yet potentially defective boundary in the green body and ultimately evolving into a delamination in sintered ceramic. Without systematically addressing the origins and evolution of these interlayer weaknesses, performance enhancements will encounter bottlenecks.

This study aims to introduce a novel perspective by reconceptualizing the interlayer zone as a dynamic evolutionary system that encompasses the VPP process, from stereolithography to sintering. The final mechanical properties are dictated by the cross-process evolution of the interlayer, governed by the synergistic interplay between photopolymerization dynamics and sintering kinetics, specifically within this zone. Instead of passively minimizing defects, we propose an active strategy of cross-process synergistic control to facilitate interlayer evolution. Specifically, an orthogonal experimental design is employed to optimize the key stereolithographic parameters, including irradiance, exposure time, and slicing thickness, to enhance the flexural strength and density by ensuring strong interlayer bonding. A particular emphasis is that layer thickness is the most pivotal factor. Subsequently, the sintering process is explored by constructing a sintering kinetic window and studying the effects of temperature and time on density, flexural strength, and microstructure evolution. This work introduces a novel cross-process synergistic control strategy aimed at guiding interlayer evolution and establishes preliminary but crucial correlations between process parameters, interlayer structural evolution, and mechanical properties.

2 Experimental

2.1 Raw material

Monoclinic ZrO_2 (m-ZrO_2; 5.85 g/cm^3, d_{50} = 0.200 μm) and tetragonal ZrO_2 (t-ZrO_2; 6.04 g/cm^3, d_{50} = 0.188 μm) powders were selected as raw ceramic powders. The volume ratio of m-ZrO_2 to t-ZrO_2 was 85 : 15. MgO (3.58 g/cm^3, > 98%) with a weight of 2 wt% for both ZrO_2 powders was used as a sintering additive. 1,6-Hexanedioldiacrylate (HDDA; 1.01 g/cm^3) and 1,1,1-trimethylol propane triacrylate (TMPTA; 1.1 g/cm^3) were mixed with a volume ratio of 4 : 1 to use as photosensitive resin monomers. A polymeric compound dispersant with a weight of 2 wt% for ZrO_2 ceramic powders, KOS110, was added to improve the rheological and printing properties of the ZrO_2 ceramic suspension. Diphenyl (2,4,6-trimethylbenzoyl) phosphine oxide (TPO; 1.17 g/cm^3) with a weight of 1 wt% for photosensitive resin monomers was used as a photoinitiator. The ZrO_2 ceramic suspension with a solid loading of 50 vol% was subjected to ball milling at a speed of 400 r/min for 12 h according to our previous work [22]. Finally, a homogeneous and stable ZrO_2 ceramic suspension was obtained.

2.2 VPP process

In this work, DLP equipment with an ultraviolet light wavelength of 405 nm was employed to fabricate ZrO_2 green bodies. Three stereolithographic process parameters, including irradiance, exposure time, and slicing thickness, were set according to the curing property of the ZrO_2 ceramic suspension. This work employed an L16 (4^3) orthogonal experimental design to investigate the stereolithographic process of ZrO_2 ceramics. The experimental factors are listed in Table 1. The specific orthogonal experimental design adopted is listed in Table 2, comprising a total of 16 groups. The ZrO_2 green bodies were then fabricated using the DLP process according to the orthogonal experimental design. Finally, ZrO_2 green bodies were ultrasonically cleaned with ethanol to remove uncured resin from their surface.

2.3 Debinding and sintering

The VPP-prepared ZrO_2 green body contains approximately 50 vol% non-ceramic components, such as cured photosensitive resin, uncured photosensitive resin monomer, and dispersant. Therefore, a gradual debinding rate must be employed to improve the formation of defects, such as cracks and delamination. In our previous study, the thermogravimetric analysis results of the cured photosensitive resin were discussed [23]. The debinding heating

Table 1 Orthogonal experimental factors for stereolithographic process parameters of ZrO_2 ceramic

Level	Factor		
	A	B	C
	Irradiance (μW/cm^2)	Exposure time (s)	Slicing thickness (μm)
1	6000	4	25
2	9000	5	50
3	12,000	6	75
4	15,000	7	100

rate was set at 0.5 °C/min and then debinded at 550 °C for 2 h. The heating rate was set at 5 °C/min and then presintered at 1000 °C for 2 h. For this orthogonal optimization of the stereolithographic parameters, the thermal treatment (debinding and sintering) was kept constant for all samples at 1600 °C for 2 h.

2.4 Characterization

Initially, the irradiance of the DLP projector was measured using a calibrated ultraviolet integrating radiometer, which features a spectral sensitivity range that corresponds to the emission peak of the UV light source at a wavelength of 405 nm. The radiometer sensor was placed at the center of the building platform at the same working distance as used during printing. Measurements were taken before each set of experiments to ensure consistency. The average irradiance value was calculated from at least five independent readings across the projection area. A clean glass slide was used to characterize the curing property of the ZrO_2 ceramic suspension. The thickness of the prepared suspension should exceed 1 mm, and then the suspension was placed under the DLP ultraviolet light for photopolymerization. The uncured ceramic suspension was removed using alcohol. Finally, the curing thickness of the ZrO_2 suspension was tested using a digital micrometer. A minimum of 6 groups is required for the purpose of estimating the mean curing thickness of the ZrO_2 ceramic suspension. The relative density of the samples was measured using Archimedes' method. The three-point flexural strength of ZrO_2 ceramics was measured using an electronic mechanical testing machine with a loading rate of 0.5 mm/min. The sizes of the samples were set as 3 mm × 4 mm × 36 mm, with a span of 30 mm. A minimum of 10 samples was needed. The microstructures of the ZrO_2 ceramics were characterized by a scanning electron microscope (SEM). The linear shrinkage was determined using a digital micrometer. The prepared ZrO_2 ceramics were characterized using nanoscale X-ray computed tomography (X-CT) scanner.

3 Results and discussion

3.1 Stereolithographic process

To select appropriate stereolithographic process parameters, the curing property of the ZrO_2 ceramic suspension was first investigated. The effect of the irradiance and exposure time on the curing property of the ZrO_2 ceramic suspension is obtained, as illustrated in Fig. 1. The curing thickness increases exponentially

Table 2 Orthogonal experimental design and results for stereolithographic process of ZrO_2 ceramic

No.	Factor			Metric	
	Irradiance (μW/cm²)	Exposure time (s)	Slicing thickness (μm)	Flexural strength (MPa)	Relative density (%)
1	A_1 = 6000	B_1 = 4	C_1 = 25	239.30±23.85	94.30±0.21
2	A_1 = 6000	B_2 = 5	C_2 = 50	314.08±27.06	94.62±0.35
3	A_1 = 6000	B_3 = 6	C_3 = 75	338.09±23.81	94.77±0.32
4	A_1 = 6000	B_4 = 7	C_4 = 100	266.25±16.80	94.73±0.15
5	A_2 = 9000	B_1 = 4	C_2 = 50	302.42±19.99	93.95±0.35
6	A_2 = 9000	B_2 = 5	C_1 = 25	198.23±21.95	94.06±0.33
7	A_2 = 9000	B_3 = 6	C_4 = 100	212.92±21.11	94.60±0.18
8	A_2 = 9000	B_4 = 7	C_3 = 75	316.98±21.62	94.80±0.25
9	A_3 = 12,000	B_1 = 4	C_3 = 75	301.24±17.04	94.29±0.34
10	A_3 = 12,000	B_2 = 5	C_4 = 100	201.88±25.44	94.30±0.22
11	A_3 = 12,000	B_3 = 6	C_1 = 25	181.78±16.15	94.18±0.19
12	A_3 = 12,000	B_4 = 7	C_2 = 50	336.58±25.44	94.45±0.26
13	A_4 = 15,000	B_1 = 4	C_4 = 100	137.47±28.44	93.79±0.35
14	A_4 = 15,000	B_2 = 5	C_3 = 75	302.48±28.45	94.28±0.27
15	A_4 = 15,000	B_3 = 6	C_2 = 50	270.02±24.31	94.33±0.25
16	A_4 = 15,000	B_4 = 7	C_1 = 25	127.28±12.43	94.77±0.28

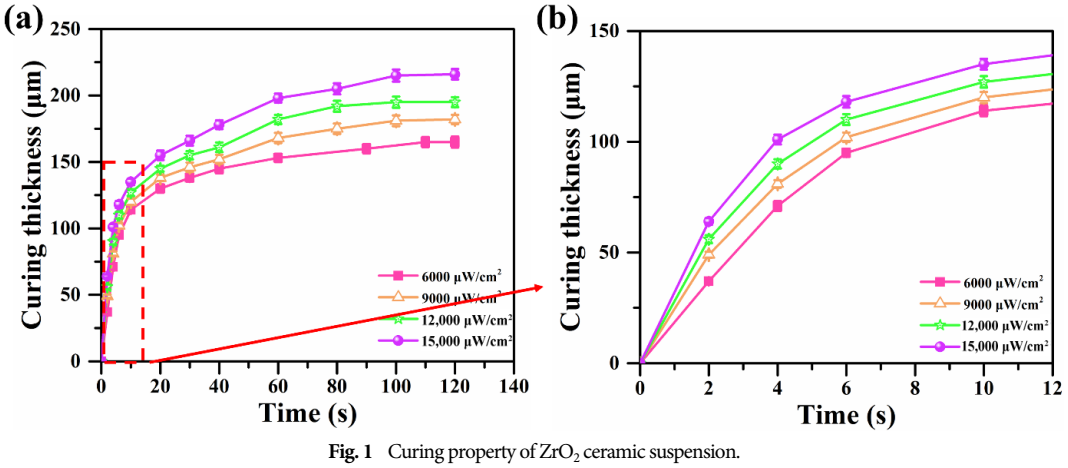

Fig. 1 Curing property of ZrO_2 ceramic suspension.

with increasing exposure time before levelling off. The curing thickness of the ZrO_2 ceramic suspension stabilizes when the exposure time exceeds 100 s. Within the same exposure time, a higher irradiance results in a greater curing thickness. This finding suggests that enhancing irradiance and prolonging exposure time can contribute to increasing the curing thickness. However, the scattering and absorption of ZrO_2 particles and the cured resin prevent the curing thickness from increasing indefinitely. Following a comprehensive analysis of the results presented in Fig. 1(b), it was determined that the exposure time would be set as 4, 5, 6, and 7 s, as listed in Table 1.

The flexural strength and relative density obtained from the orthogonal experiments are presented in Table 2. Subsequently, the range analysis method was employed to calculate these two metrics, as listed in Table 3. The factors influencing the two experimental metrics were then ranked in order of significance based on the magnitude of the range *R*. For the flexural strength of ZrO_2 ceramics, slicing thickness > irradiance > exposure time, indicating that slicing thickness exerted the greatest influence, followed by irradiance, with exposure time having the least impact. The exposure time primarily influences the secondary photopolymerization conversion rate between layers, which directly affects the interlayer bonding quality and, consequently, the relative density. However, flexural strength is more sensitive to the combined effect of irradiance and slicing thickness, which governs the primary polymerization degree and the structural uniformity across layers. While exposure time contributes to densification by enhancing interlayer bonding, its individual effect on flexural strength is less pronounced than the other two factors within the selected parameter range. The optimal combination of experimental parameters yielding maximum flexural strength is A1B4C3. This corresponds to an irradiance of 6000 μW/cm^2, an exposure time of 7 s, and a slicing thickness of 75 μm, thereby yielding the highest flexural strength for the ZrO_2 ceramic. The order of influence on relative density is as follows: exposure time > irradiance > slicing thickness. The optimal combination of A1B4C3 has been shown to yield the maximum relative density. Following a comprehensive evaluation, the experimental parameters yielding the maximum flexural strength were selected. Experimental verification confirmed that ZrO_2 ceramics manufactured using the optimal stereolithographic process parameters exhibited a flexural strength of 366.65±15.35 MPa and a relative density of 95.94%±0.12%.

This study then focuses on analyzing the effect of the irradiance, exposure time, and slicing thickness on the interlayer zone, mechanical properties, and relative density of ZrO_2 ceramics. Figure 2 illustrates the effect of irradiance on the flexural strength and relative density of ZrO_2 ceramics after sintering. Within the selected irradiance range from 6000 to 15,000 μW/cm^2, both the flexural strength and relative density of the ZrO_2 ceramic gradually decrease as irradiance increases.

Given that exposure time has minimal impact on the mechanical properties of ZrO_2 ceramics (as indicated by a range analysis deviation of 11.07 MPa), samples with consistent slicing thickness (25 μm) and varying exposure time (4, 5, 6, 7 s) were selected to examine the effects of irradiance on mechanical properties. As illustrated in Figs. 3(a)–3(d), the side surfaces (along the building direction) of the green body manifest characteristics of layer-by-layer manufacturing, accompanied by interlayer cracks (or delamination). These cracks increase in prevalence with increasing irradiance. This can be attributed to the observation that as irradiance increases, the energy input increases from 24 to 105 mJ/cm^2, and the primary photopolymerization conversion rate of the resin monomer in the cured layer rises, leading to a reduction in residual resin monomers. During subsequent photopolymerization of the curing layer, there is a reduction in the number of residual monomers available for secondary photopolymerization in the last cured layer [24]. Consequently, the formation of weak interlayer bonding results in a reduction in mechanical properties after sintering under these photothermal fields.

This results in a lower polymerization degree in the second polymerization zone and ultimately weaker interlayer bonding, as shown in Fig. 4. This is particularly evident at the edges, where the ZrO_2 ceramic green body is subjected to vacuum force from the release film. Such weak interlayer bonding induces interlayer cracks, which in turn increase the risk of delamination defects after sintering. These weaker interlayer bonds and cracks at the edges are not susceptible to elimination during the sintering processes (Figs. 3(e)–3(h)). Instead, they will become origins of structural failure, leading to a reduction in the flexural strength of the ZrO_2 ceramic. Concurrently, as irradiance increases, the curing degree at interlayer interfaces decreases, resulting in weak interlayer bonding. Consequently, the bulk density of ceramic particles decreases, leading to a corresponding reduction in density after sintering under these photothermal fields. It is important to note that as the selected energy input achieves a curing thickness that exceeds the slicing thickness, surface cracks on the ZrO_2 ceramic green body do not necessarily extend into the interior.

Table 3 Orthogonal experimental result analysis for stereolithographic process of ZrO_2 ceramic

Metric	Mean/range	Factor		
		Irradiance (μW/cm^2)	Exposure time (s)	Slicing thickness (μm)
Flexural strength (MPa)	K_1	289.43	245.11	186.65
	K_2	257.64	247.98	305.78
	K_3	249.18	250.70	314.70
	K_4	209.31	261.77	198.44
	R	80.12	11.07	128.05
Relative density (%)	K_1	94.60	94.08	94.33
	K_2	94.35	94.32	94.34
	K_3	94.31	94.47	94.53
	K_4	94.29	94.69	94.36
	R	0.31	0.61	0.20

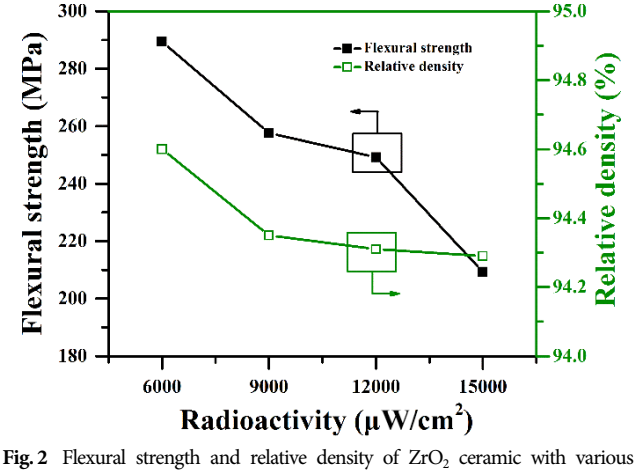

Fig. 2 Flexural strength and relative density of ZrO_2 ceramic with various irradiance levels.

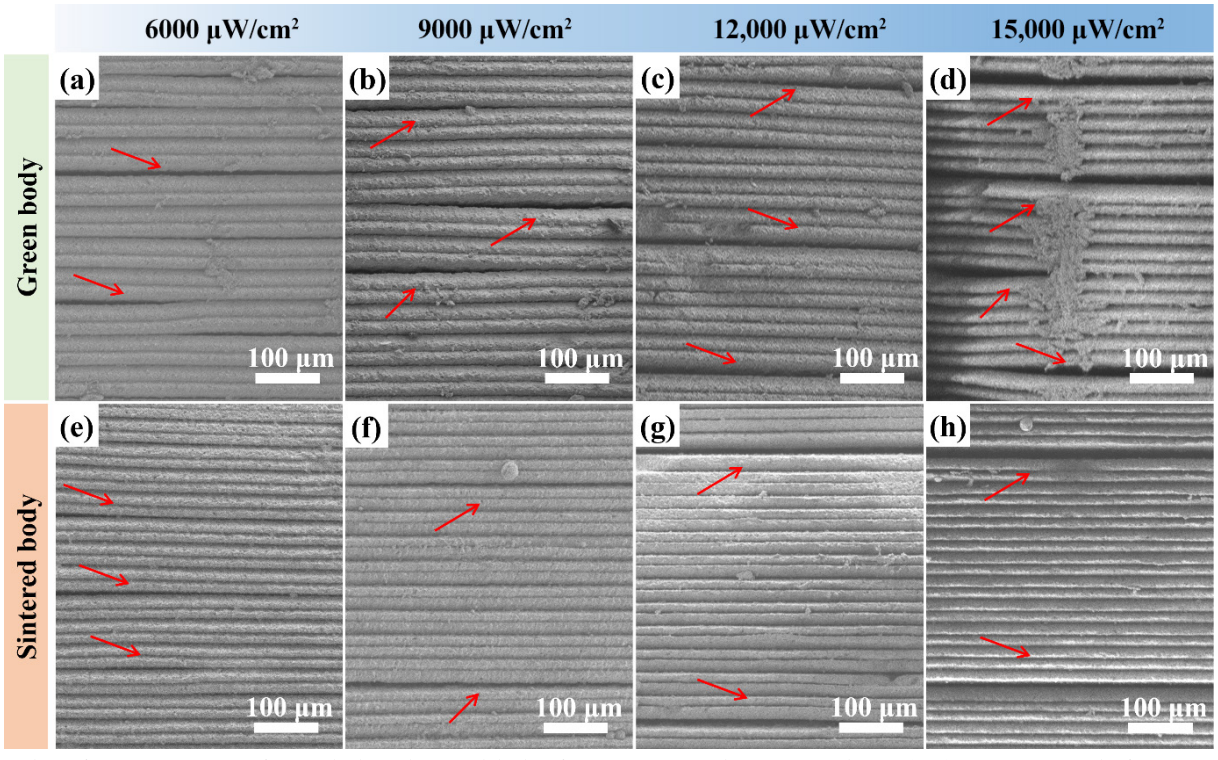

Fig. 3 Side surface microstructure of green body and sintered body of ZrO_2 ceramic with various irradiance: (a, e) 6000 μW/cm²; (b, f) 9000 μW/cm²; (c, g) 12,000 μW/cm²; and (d, h) 15,000 μW/cm².

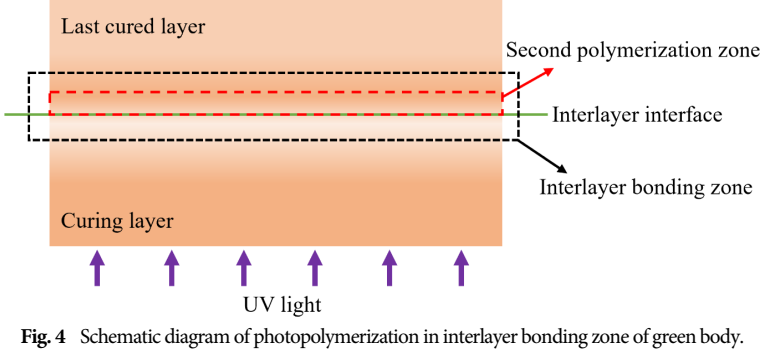

Fig. 4 Schematic diagram of photopolymerization in interlayer bonding zone of green body.

Figure 5 shows the effect of the exposure time on the flexural strength and relative density of the sintered body of ZrO_2 ceramic. It has been demonstrated that with increasing exposure time in the range from 4 to 7 s, both the flexural strength and relative density of the sintered body of ZrO_2 ceramic increase. As demonstrated by the side surface morphology of the green bodies of ZrO_2 ceramic in Figs. 6(a)–6(d), the interlayer defects decreased progressively as the exposure time increased from 4 to 7 s. Considering that irradiance has a minimal effect on the mechanical properties of ZrO_2 ceramics, as evidenced by a range analysis deviation of 80.12 MPa compared with 128.05 MPa for slicing thickness, samples with a consistent slicing thickness of 100 μm, while varying the irradiance levels (15,000, 12,000, 9000, and 6000 μW/cm²) were selected to investigate the effects of exposure time on mechanical properties. Within a shorter exposure time, due to the higher irradiance, the primary photopolymerization conversion rate of the photosensitive resin monomers is relatively high. Despite the presence of a substantial amount of residual monomer, the energy input (irradiance and exposure time) still proves to be a high energy input (60 mJ/cm²). Consequently, the secondary photopolymerization conversion rate of the residual resin monomers in the last cured layer remains

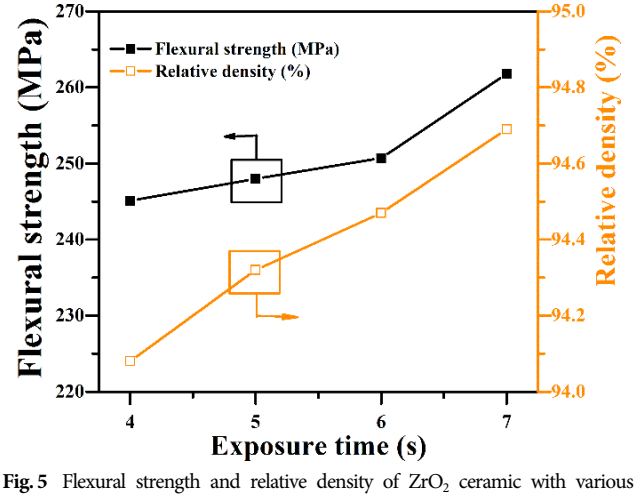

Fig. 5 Flexural strength and relative density of ZrO_2 ceramic with various exposure time.

low, which is attributed to the weak interlayer bonding. Therefore, during the lifting process on the platform of the DLP, the vacuum force exerted by the release film was observed to induce the

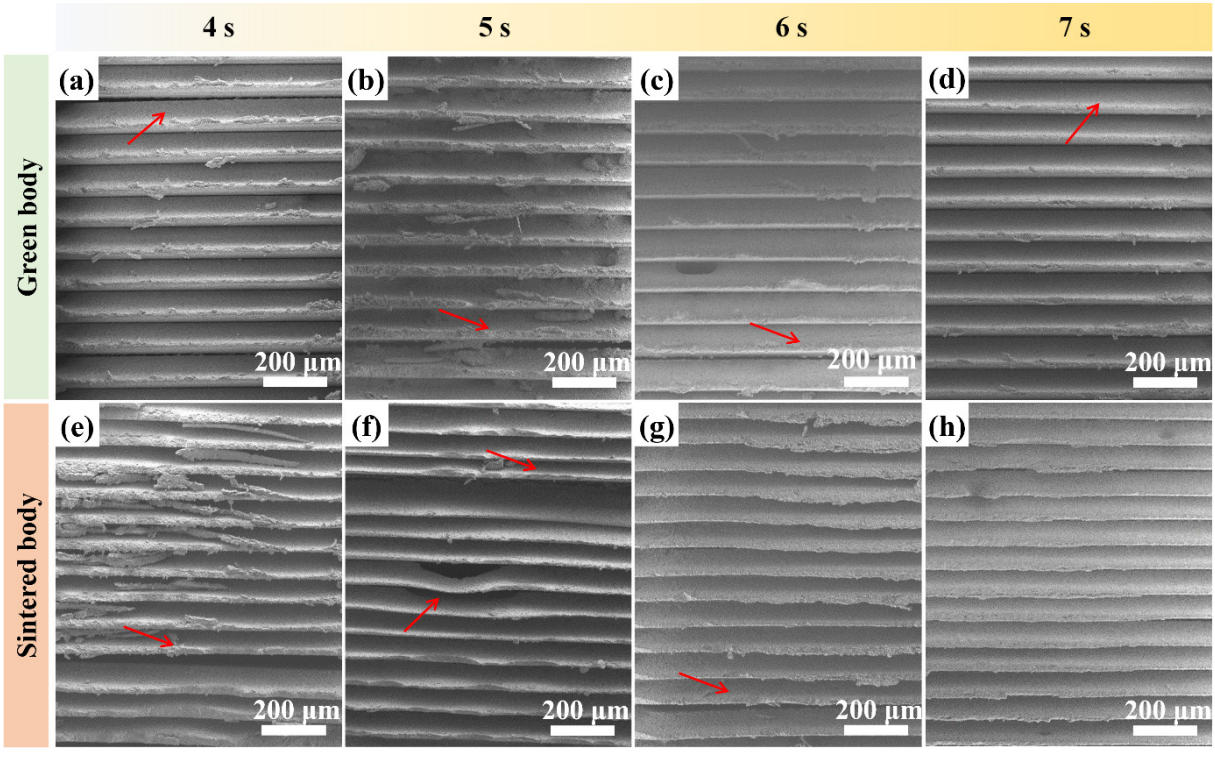

Fig. 6 Side surface microstructure of green body and sintered body of ZrO_2 ceramic with various exposure time: (a, e) 4 s; (b, f) 5 s; (c, g) 6 s; and (d, h) 7 s.

formation of interlayer cracks at the outer surface edges of the ZrO_2 ceramic green body (Fig. 6(a)). As the curing thickness exceeds the slicing thickness due to the high energy input, these interlayer cracks do not propagate into the interior of the green body, thus avoiding delamination defects. However, this weak interlayer bonding becomes highly susceptible to delamination defects after sintering, resulting in a reduction in mechanical properties. As the exposure time increases, the primary photopolymerization conversion rate of the photosensitive resin gradually rises, and the energy input decreases from 60 to 42 mJ/cm^2 due to the irradiance decrease, accompanied by an increase in the secondary photopolymerization conversion rate. This process enhances the interlayer bonding and reduces the formation of defects between the two cured layers (Figs. 4 and 6(b)–6(d)). Consequently, interlayer defects decrease after sintering (Figs. 6(e)–6(h)), and the flexural strength and relative density of the ZrO_2 ceramic increase.

As shown in Fig. 7, both the flexural strength and relative density of the ZrO_2 ceramic initially increase with slicing thickness, reaching a maximum at 75 μm, and then decrease at 100 μm. This trend can be explicitly linked to the photopolymerization mechanisms discussed earlier. Considering that exposure time has a minimal effect on the mechanical properties of ZrO_2 ceramics, as evidenced by a range analysis deviation of 11.07 MPa compared with 80.12 MPa for irradiance, samples with a consistent irradiance of 6000 μW/cm^2 were selected, while varying the exposure time (4, 5, 6, and 7 s) to investigate the effects of exposure time on mechanical properties. The side surface microstructure for the green bodies of ZrO_2 ceramic is illustrated in Figs. 8(a)–8(d). When the slicing thickness of 25 μm is minimal, the primary photopolymerization conversion rate of the photosensitive resin is elevated due to the relatively thin layer, resulting in overcuring (the energy input is 24 mJ/cm^2). The resultant scarcity of residual monomers has been demonstrated to limit the secondary photopolymerization conversion rate during subsequent layer curing, which is insufficient to ensure strong

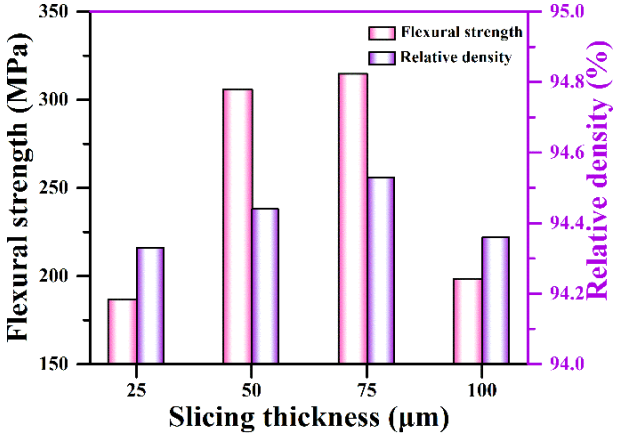

Fig. 7 Flexural strength and relative density of ZrO_2 ceramic with various slicing thicknesses.

interlayer bonding. Consequently, interlayer defects and strength reduction occur (Fig. 8(a)). As the slicing thickness increases to 50 μm and further to 75 μm, the energy input increases from 24 to 36 mJ/cm^2, and primary photopolymerization becomes more complete, resulting in sufficient residual monomers. These residual monomers undergo secondary photopolymerization with the resin of the subsequent layer under UV light, achieving an optimal balance between primary and secondary conversion that avoids both insufficient polymerization and overcuring. This results in strong interlayer bonding and reduced interlayer defect occurrence (Figs. 8(c) and 8(g)), thereby enhancing flexural strength. However, at a slicing thickness of 100 μm, although the energy input is 42 mJ/cm^2, the primary photopolymerization conversion rate of the photosensitive resin becomes too low due to the increased layer thickness. Despite the presence of a greater quantity of residual monomers, inadequate energy input results in a low secondary photopolymerization conversion rate between the subsequent layer and these residual monomers, resulting in weak

interlayer bonding and the reappearance of interlayer defects after sintering (Figs. 8(d) and 8(h)). This mechanistic interpretation aligns with the interlayer bonding models proposed in Fig. 9, where moderate primary conversion with sufficient residual monomers leads to strong interlayer bonding (Fig. 9(b)), while either insufficient or excessive conversion results in weak bonding (Figs. 9(a) and 9(c)). This phenomenon consequently results in a decline in the interlayer bonding of the green body. Interlayer defects in the ZrO_2 ceramic were observed after sintering. Consequently, interlayer defects exhibited an initial increase and then a decrease with increasing slicing thickness under photothermal fields (Figs. 8(e)–8(h)). Therefore, the strength of the ZrO_2 ceramic also initially increases and then decreases.

In general, three interlayer bonding models may be present in VPP additive manufactured ceramic green bodies: (1) Due to inadequate energy input, specifically low irradiance and short exposure time, primary photopolymerization yields a low conversion rate with abundant residual resin monomers in the first cured layer. However, secondary photopolymerization also remains insufficient, resulting in weak interlayer bonding in the green body (Fig. 9(a)). It can lead to defects such as cracks, resulting in low strength of the ceramic after sintering under a photothermal field. (2) With sufficient energy input, i.e., appropriate irradiance and adequate exposure time, the primary photopolymerization conversion rate is high in the first cured layer. This also leaves sufficient residual resin monomers for secondary photopolymerization, resulting in strong interlayer bonding in the green body (Fig. 9(b)). It will enhance the strength of the ceramic after sintering under a photothermal field. (3) Due to high energy input, such as high irradiance and long exposure time, the conversion rate of primary photopolymerization is extremely high. This leaves few residual resin monomers in the

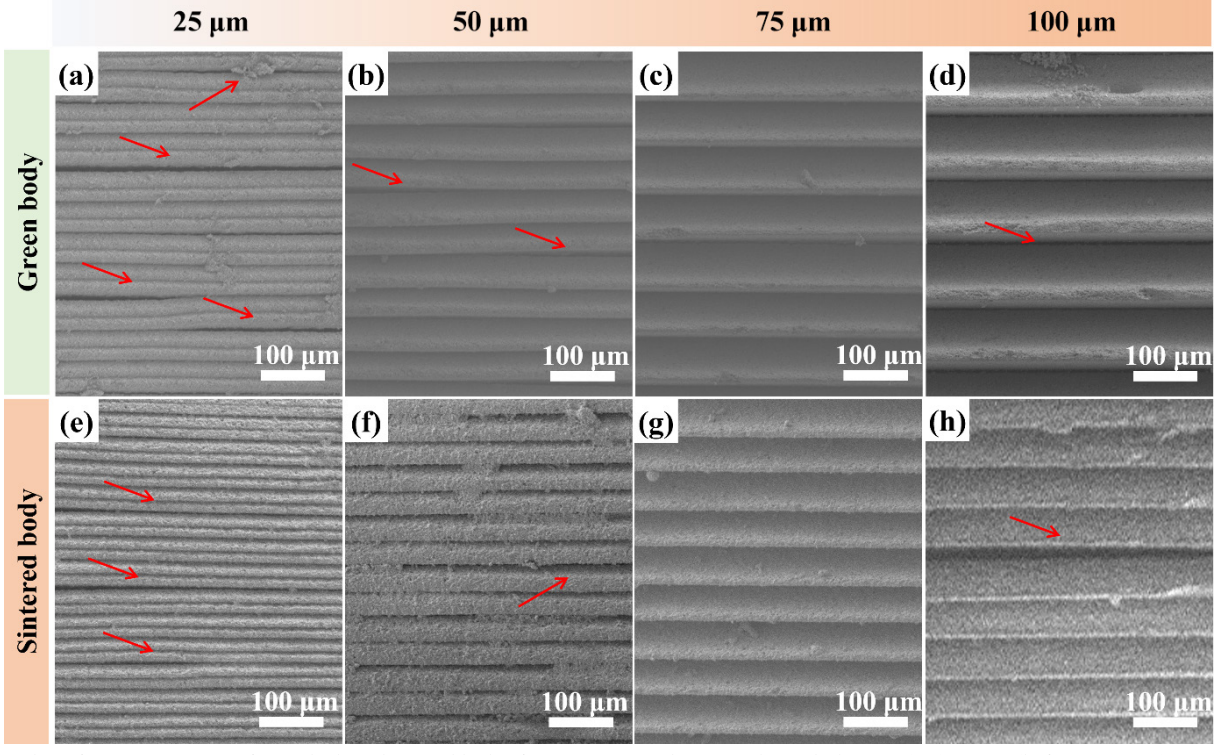

Fig. 8 Side surface microstructure of green body and sintered body of ZrO_2 ceramic with various slicing thicknesses: (a, e) 25 μm; (b, f) 50 μm; (c, g) 75 μm; and (d, h) 100 μm.

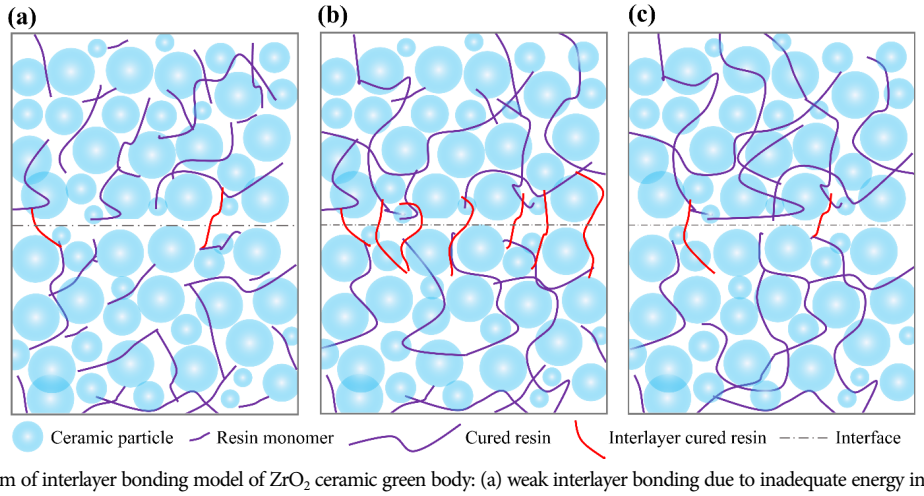

Fig. 9 Schematic diagram of interlayer bonding model of ZrO_2 ceramic green body: (a) weak interlayer bonding due to inadequate energy input, (b) strong interlayer bonding due to sufficient energy input, and (c) weak interlayer bonding due to high energy input.

清華大学出版社 Tsinghua University Press | SciOpen

first cured layer. The insufficient quantity of monomers for secondary photopolymerization results in weak interlayer bonding in the green body (Fig. 9(c)). Similarly, ceramics have relatively low strength.

Therefore, to manufacture a ZrO_2 ceramic with high mechanical properties, it is essential to ensure strong interlayer bonding to reduce the risk of delamination and crack defects. Achieving an appropriate primary photopolymerization conversion rate is essential in this process, while ensuring that a sufficient residual resin monomer is present for secondary photopolymerization to form strong interlayer bonding. Consequently, the selection of irradiance, exposure time, and slicing thickness must be mutually compatible. This systematic investigation of the stereolithographic process for ZrO_2 ceramic has determined the optimal stereolithographic parameters to be as follows: an irradiance of 6000 μW/cm^2, an exposure time of 7 s, and a slicing thickness of 75 μm. The microstructure of the prepared ZrO_2 ceramic is illustrated in Fig. 10. The absence of crack defects on the side surfaces of the green bodies before and after sintering serves to validate the conclusions previously outlined. To provide further confirmation of the decisive influence of precisely controlling the dynamic balance between primary and secondary conversion rates on internal interlayer behavior, X-CT technology was employed to verify that internal interlayer crack defects were eliminated under photothermal fields (Fig. 10(c)). As demonstrated in Fig. 1(b), the slicing thickness of the ZrO_2 ceramic suspension under this energy input is 100 μm. Consequently, within the specified parameters, when the curing thickness exceeds the slicing thickness by approximately 25 μm, the primary photopolymerization conversion rate of the cured layer is optimal. This process ensures the presence of sufficient residual resin monomers for secondary photopolymerization in the interlayer. Following secondary photopolymerization, adequate interlayer bonding strength is achieved, thereby preventing interlayer defects in the green body and after sintering (Figs. 4, 9(b), and 10). This process effectively enhances the strength of the ceramic. Conversely, an inadequate or superfluous energy input will engender insufficient or excessive secondary polymerization conversion rates. The weak interlayer bonding will lead to interlayer cracking after the sintering process, resulting in reduced strength of the ceramic. In the future, we will focus on the quantitative characterization of primary and secondary photopolymerization conversion rates of the resin monomer, achieving optimal interlayer bonding strength to ultimately produce defect-free ceramics.

3.2 Sintering process

Although the delamination defects were eliminated, pore defects were observed in the sintered bodies and must still be controlled, as shown in Fig. 10(c). The presence of pore defects in the interlayer zone decreases the mechanical properties of the ceramics. Therefore, it is necessary to control interlayer pore defects across the manufacturing process. Apart from photopolymerization dynamics, sintering kinetics have the most significant impact on pore defects during ceramic manufacturing. Next, this work aims to exploit the interaction between interlayer photopolymerization dynamics and sintering kinetics to control pore defects more effectively and improve the mechanical properties of ceramics. In particular, the evolution of interlayer pores, originating from weak interlayer bonding during printing, is strongly influenced by sintering temperature. Understanding how these pores close or persist during thermal treatment is key to enhancing the final microstructure and mechanical performance.

The sintering kinetic window of ZrO_2 ceramic (the same stereolithographic parameters: an irradiance of 6000 μW/cm^2, an exposure time of 7 s, and a slicing thickness of 75 μm) was first explored. The effects of sintering temperatures at 1200–1650 °C for 2 h on the flexural strength, relative density, and microstructure were examined, as illustrated in Figs. 11(a) and 12. In classical sintering theory, the initial stage is predominantly characterized by particle rearrangement (e.g., grain slip and rotation). The subsequent stage is dominated by cooperative particle rearrangement and atomic diffusion, which marks the commencement of grain growth. However, this growth is relatively slow, as illustrated in Figs. 12(a)–12(d) and 12(l). As demonstrated in the microstructure (Fig. 12(d)), open pores disappear at approximately 1350 °C, leaving closed pores in the sintered body. These residual pores are predominantly located in interlayer regions, where incomplete photopolymerization during printing leads to locally lower green density. During sintering, these interlayer pores require higher thermal activation to close due to reduced particle coordination and limited diffusion pathways. Although the process of grain growth is not rapid during this stage, the rapid expulsion of open pores leads to a significant increase in relative density. It is noteworthy that in the sintering of conventionally manufactured ceramics, the relative density corresponding to the temperature at which open pores disappear is typically approximately 93% of the theoretical density [25]. In contrast, the relative density recorded in this study was approximately 89.59%, reflecting the persistence of interlayer porosity and the need for tailored sintering strategies to overcome this limitation. As previously mentioned, defects form in the building direction of ceramics due to weak interlayer bonding, leading to a reduction in the relative density of ZrO_2 ceramics. As demonstrated in Figs. 12(e)–12(k), when the temperatures exceed 1350 °C, although grains undergo accelerated growth and pores

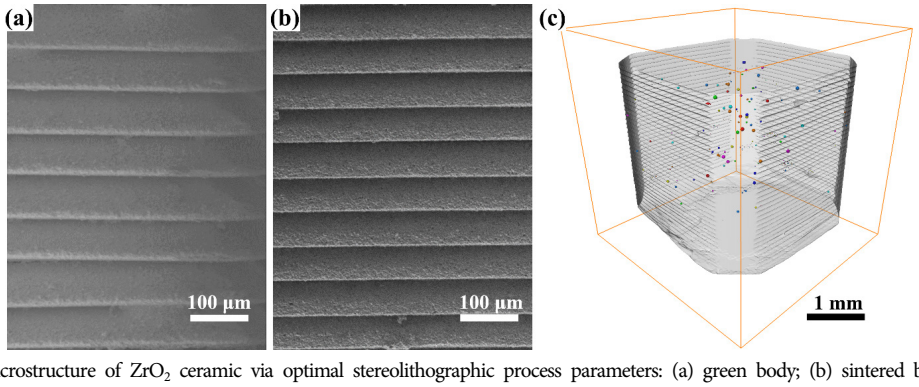

Fig. 10 Side surface microstructure of ZrO_2 ceramic via optimal stereolithographic process parameters: (a) green body; (b) sintered body; and (c) 3D X-CT reconstructed images of sintered body.

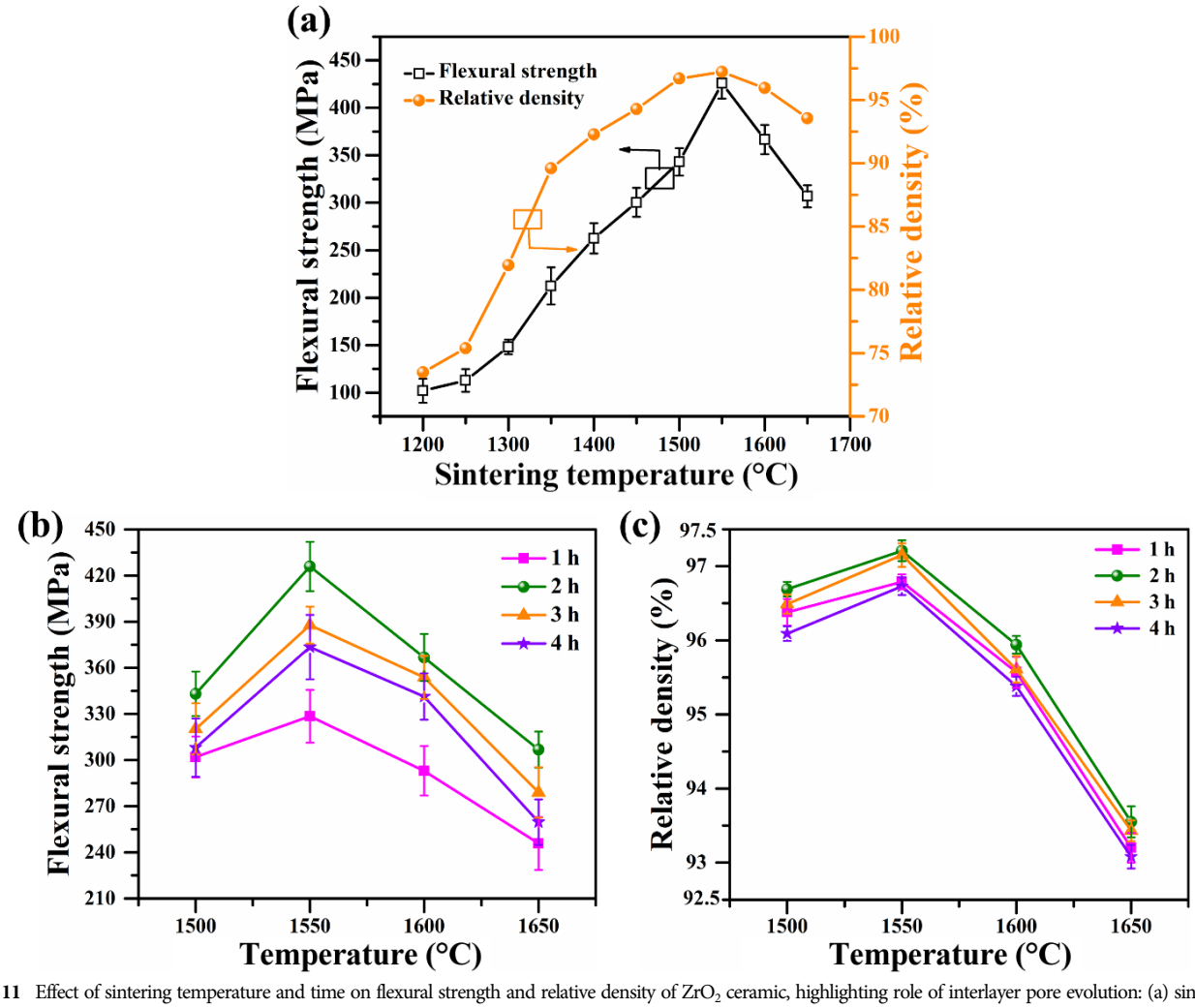

Fig. 11 Effect of sintering temperature and time on flexural strength and relative density of ZrO_2 ceramic, highlighting role of interlayer pore evolution: (a) sintering kinetic window, (b) flexural strength, and (c) relative density.

attached to grain boundaries are expeditiously expelled via grain boundary diffusion, a minute proportion persists at the grain boundaries (Figs. 12(g) and 12(h)). As the majority of pores are expelled, the rate of relative density decrease slows. As sintering temperatures increase, atomic diffusion plays a pivotal role in the process of grain growth. Furthermore, it has been demonstrated that interfacial atomic diffusion and particle rearrangement jointly accelerate densification. This phenomenon is indicative of enhanced intergranular contact, resulting in the substantial elimination of residual pores, thereby leading to the formation of a compact grain structure. At a temperature of 1550 °C, the pores at the grain boundaries are significantly expelled, resulting in peak values of flexural strength and relative density (Fig. 12(i)). When the temperature is higher than 1550 °C, abnormal grain growth occurs. Pores are unable to be expelled promptly, leading to a decrease in relative density and then deterioration in flexural strength (Figs. 12(j) and 12(k)). This phenomenon can be attributed to the occurrence of excessive sintering, which in turn induces inappropriate interfacial atomic diffusion. Consequently, this accelerates grain boundary migration beyond the void migration rate. Voids affixed to grain boundaries are unable to keep pace with boundary movement, resulting in their entrapment in the grains. Concurrently, the occurrence of abnormal grain growth gives rise to a nonuniform microstructure, resulting in a reduction in the relative density and flexural strength. As demonstrated in Fig. 12(f), a diffusion process occurs whereby fine grains become intertwined with larger grains through the parent lattice. The total grain boundary area of the system decreases, thereby reducing the total free energy. In contrast, during the initial grain growth stage, curved grain boundaries exhibit higher curvature and greater motility, moving at relatively high speeds. This phenomenon results in the entrapment of voids in the grains, hindering their migration to boundaries [26].

To obtain the optional sintering process parameters of ZrO_2 ceramic, the effects of sintering temperature and time on the flexural strength and relative density of ZrO_2 ceramics were systematically investigated. The presintered bodies were sintered at 1500, 1550, 1600, and 1650 °C for 1, 2, 3, and 4 h, respectively. The results are presented in Figs. 11(b) and 11(c). At equivalent dwell time, both the flexural strength and relative density of the ZrO_2 ceramics exhibited an initial increase and then a decrease with increasing sintering temperature. The maximum flexural strength and relative density were obtained at 1550 °C. Conversely, at a constant sintering temperature, both flexural strength and relative density exhibited an initial increase and then a decrease with increasing dwell time. A maximum flexural strength of 425.89±16.01 MPa and a relative density of 97.21%±0.14% were obtained at a sintering temperature of 1550 °C and a dwell time of 2 h via this effective cross-process synergistic control for interlayer bonding under a photothermal field. During the solid-state sintering process, an increase in

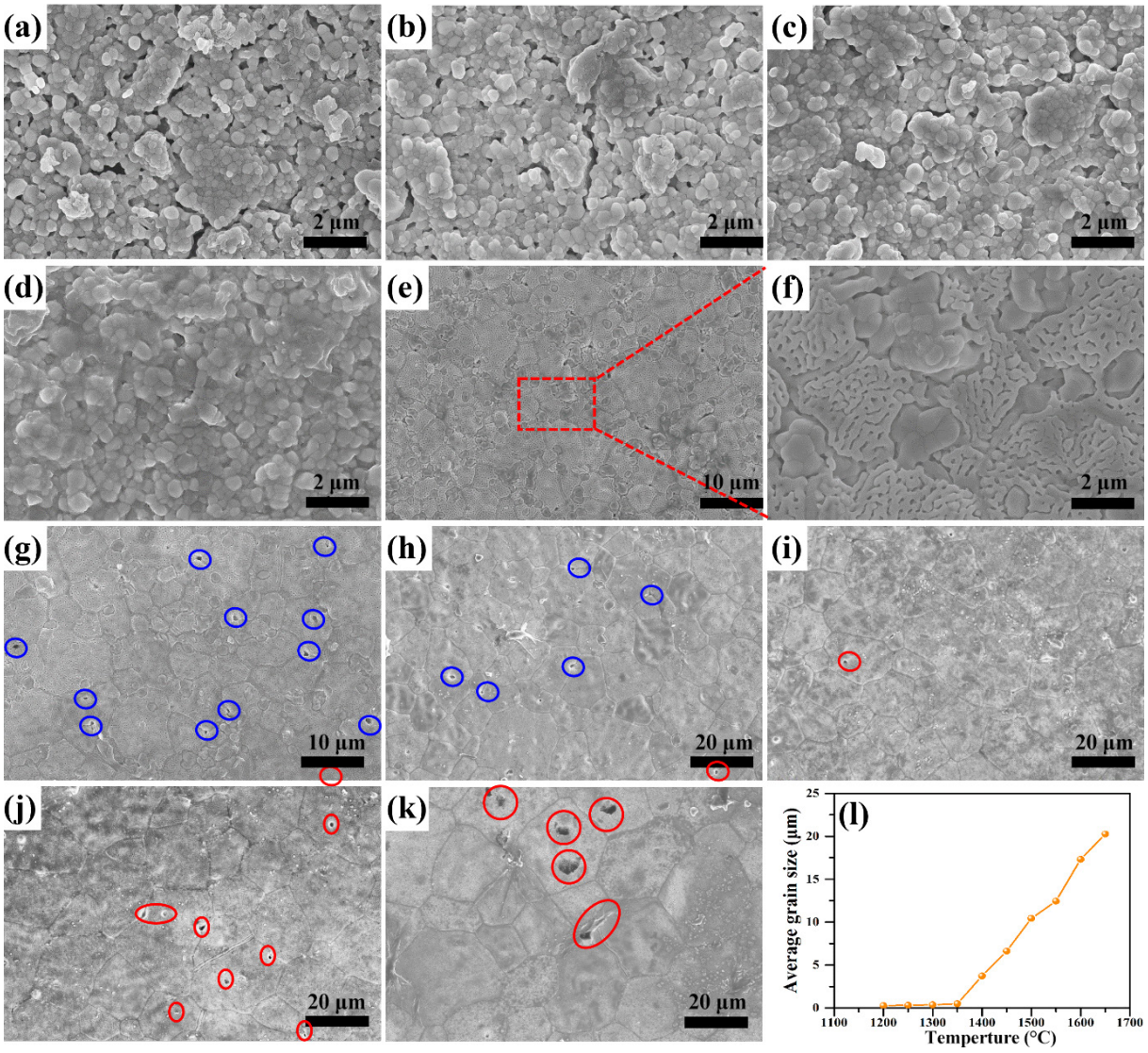

Fig. 12 Microstructure of ZrO_2 ceramic sintered at various temperatures for 2 h: (a) 1200 °C, (b) 1250 °C, (c) 1300 °C, (d) 1350 °C, (e, f) 1400 °C, (g) 1450 °C, (h) 1500 °C, (i) 1550 °C, (j) 1600 °C, (k) 1650 °C; and (l) grain size.

energy availability is observed with increasing sintering temperature, thereby promoting the densification of the ZrO_2 ceramic. The migration rate of grain boundaries is found to exceed that of internal pores, thus enabling grain boundaries to detach from voids and move freely. This process is accompanied by grain coalescence in the ZrO_2 ceramic, which in turn results in the simultaneous trapping of additional pores in the grains. These residual pores prove difficult to contract, expel, or eliminate during the final stages of sintering, consequently reducing the relative density and flexural strength of the ZrO_2 ceramic [26].

For context, conventional sintering of ZrO_2 ceramics typically involves temperatures ranging from 1400 to 1600 °C with dwell time of 2–4 h, depending on the stabilizer content and initial green density. In comparison, the optimal sintering conditions identified in this study (1550 °C for 2 h) fall well within this conventional range, indicating that VPP-fabricated ZrO_2 green bodies can achieve full densification under thermal schedules comparable to those used for conventionally compacted ceramics. However, it is noteworthy that the relative density achieved here (~97.2%) is slightly lower than the near-theoretical densities (> 99%) often reported for conventionally sintered ZrO_2. This discrepancy is attributed to residual interlayer pores inherited from the layer-wise VPP process, which are more difficult to eliminate than uniformly distributed pores in conventionally pressed compacts. These findings underscore the importance of not only optimizing sintering parameters but also improving interlayer bonding during photopolymerization to further enhance densification.

As illustrated in Fig. 13, the effect of dwell time at a sintering temperature of 1550 °C on the microstructure of ZrO_2 ceramics is demonstrated. When the dwell time is 1 h, numerous pore defects in the ZrO_2 ceramic remain trapped and cannot be expelled or eliminated (Fig. 13(a)). As the dwell time increases, ZrO_2 ceramic grains continue to grow, while the curvature of grain boundaries and the driving force for grain boundary motion gradually decrease. Pores entrapped in grain boundaries undergo a progressive migration to the boundaries, ultimately leading to their disappearance, thereby resulting in a gradual reduction in pore defects (Fig. 12(b)). Prolonged time also leads to abnormal grain growth in the ZrO_2 ceramic, promoting pore coalescence and enlargement of internal voids (Figs. 12(c)–12(e)). Consequently, the relative density and flexural strength of the ZrO_2 ceramic decrease as time increases.

The effect of the sintering temperature and dwell time on the

linear shrinkage of the ZrO_2 ceramic is illustrated in Fig. 14. The shrinkage behavior of ZrO_2 ceramic green bodies exhibits anisotropy, and the linear shrinkage in the *x*- and *y*-directions is similar but lower than that in the *z*-direction (along the building direction). This phenomenon can be attributed primarily to the weak interlayer bonding present in the building direction, which leads to increased shrinkage in the *z*-direction after sintering [27]. Concurrently, the constraints imposed by the firing plate on the samples result in reduced shrinkage in the *x*- and *y*-directions. As the sintering temperature increases, the linear shrinkage initially rises before falling, a phenomenon that is primarily related to sintering densification. The effect of dwell time on linear shrinkage is relatively minor. At a sintering temperature of 1550 °C and a dwell time of 2 h, the linear shrinkage of the ZrO_2 ceramic in the *x*-, *y*-, and *z*-directions is 18.77%±0.13%, 18.99%±0.18%, and 19.95%±0.09%, respectively.

As illustrated in Fig. 15, a comparative analysis is presented between the relative density and flexural strength of ZrO_2 ceramic produced via VPP in this study and those reported in Refs. [17,21,28–34]. The flexural strength of the ZrO_2 ceramic obtained in this study reaches a relatively high level in comparison to previous research, owing to the effective cross-process synergistic control for the interlayer bonding under a photothermal field. The relative density of the ZrO_2 ceramic in this study is 97.21%±0.14%, which is slightly lower than the highest values reported in some previous studies (e.g., > 99% in Refs. [31–34]). This discrepancy is primarily attributed to residual interlayer micropores that were not fully eliminated during sintering. A brief comparative overview of the relative density and flexural strength from the references is provided in Fig. 15, highlighting the trade-off between densification and mechanical performance in VPP-fabricated ZrO_2 ceramics. This discrepancy is primarily attributable to inadequate control of internal defects (e.g., interlayer pores) in the ZrO_2 ceramic. Future research efforts aimed at eliminating these internal defects have the potential to significantly improve the density and flexural strength of ZrO_2 ceramics. For instance, integrating HIP after presintering could effectively close residual interlayer pores by applying isostatic pressure at elevated temperatures, thereby promoting grain boundary diffusion and pore elimination [21]. Moreover, refining the debinding schedule, such as extending hold time at critical decomposition temperatures or using oxidative atmospheres, may reduce gas entrapment and minimize pore formation. These approaches, when coupled with the interlayer-focused process control proposed in this study, offer a pathway toward fully dense, high-strength ceramic components.

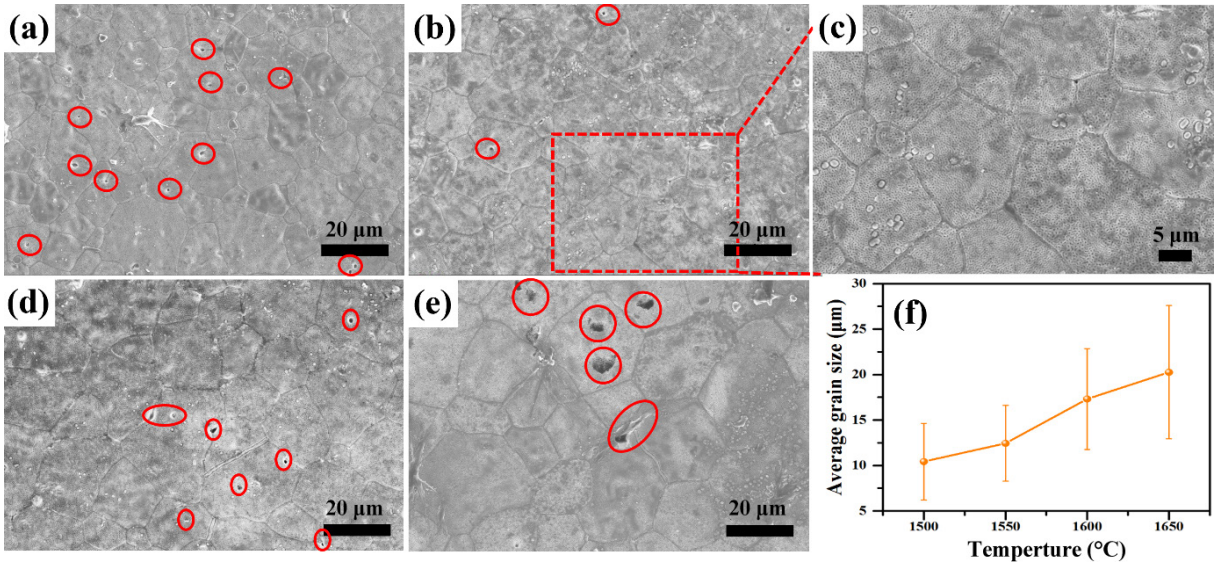

Fig. 13 Microstructure of ZrO_2 ceramic sintered at 1550 °C for various dwell time: (a) 1 h, (b, c) 2 h, (d) 3 h, (e) 4 h; and (f) grain size.

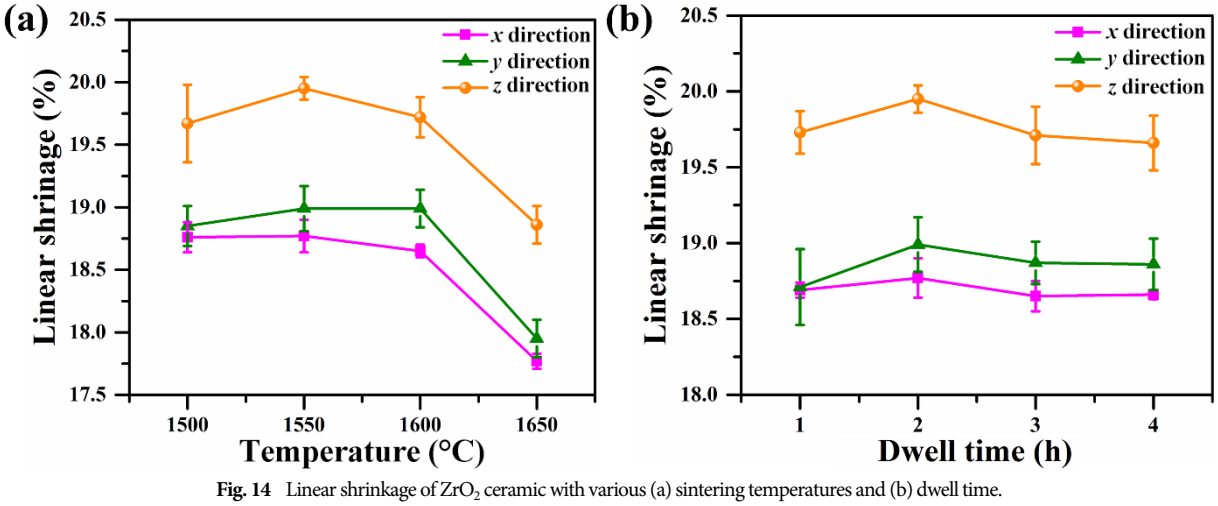

Fig. 14 Linear shrinkage of ZrO_2 ceramic with various (a) sintering temperatures and (b) dwell time.

清華大学出版社 Tsinghua University Press | SciOpen

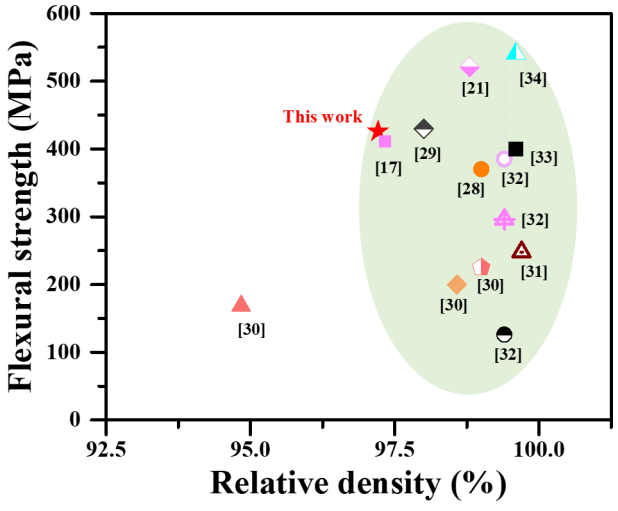

Fig. 15 Ashby plots comparing mechanical properties of VPP additive manufactured ZrO_2 in this work with those reported in Refs. [17,21,28–34].

4 Conclusions

In conclusion, this study advances the paradigm for enhancing the performance of VPP additive manufactured ceramics by transitioning from the optimization of individual steps in the process to an integrated approach that focuses on interlayer bonding. By reconceptualizing the interlayer as a dynamic system that evolves continuously through stereolithography and sintering, we address the performance limitation inherent in its cross-process evolution under a coupled photothermal field.

The orthogonal experimental analysis reveals that slicing thickness is the most decisive parameter in the stereolithographic process. The mechanical properties of the final ceramic are not merely limited by process-specific defects but are primarily determined by the synergistic interaction between photopolymerization kinetics and sintering dynamics in the interlayer. The green body demonstrated strong interlayer bonding in the green body through the effective dynamic balance of primary and secondary photopolymerization. Subsequent tailored sintering enhances the densification of the interlayer microstructure by improving the particle packing density, thereby actively strengthening the structural integrity rather than merely addressing the defect. Furthermore, the results demonstrate that interlayer pores originating from the layer-by-layer printing process can be effectively minimized by sintering within a well-defined temperature window (1350–1550 °C), where grain boundary diffusion and pore migration are optimally balanced. Using the optimized parameters (irradiance: 6000 μW/cm^2, exposure time: 7 s, layer thickness: 75 μm), the ZrO_2 ceramics exhibit outstanding performance, yielding a flexural strength of 425.89±16.01 MPa and a relative density of 97.21%±0.14% after sintering at 1550 °C for 2 h, which validates the efficacy of our approach.

The principal contributions of this work are twofold. First, it presents a concrete and effective processing method for the fabrication of high-performance ZrO_2 ceramics via VPP. Second, it proposes a novel framework that establishes relations between process parameters, interlayer structural evolution and mechanical properties. This work enhances our understanding of property development in VPP additive manufactured ceramics and paves the way for the integrated design of processes applicable to other material systems where an interlayer is essential. Future research should focus on the *in situ* monitoring of interlayer evolution to validate the proposed photopolymerization dynamics model. This could be achieved by employing techniques such as *in situ* infrared thermal imaging to observe exothermic reactions and detect defect formation during printing and *in situ* X-ray diffraction (XRD) to track phase transformations and stress development during the sintering process. Integrating these characterization methods with the present synergistic control strategy would allow for real-time feedback and adaptive process control, paving the way for its extension to more complex geometries and multimaterial architectures. In particular, to further address the residual porosity observed in the interlayer regions, future efforts could explore pressure-assisted sintering techniques such as two-step sintering or HIP, which has been shown to effectively close residual pores and enhance mechanical properties. Additionally, optimizing the binder burnout process may reduce pore formation originating from organic decomposition. These strategies, combined with the cross-process synergistic control proposed in this work, hold promise for achieving near-full densification and further improving the performance of VPP additive manufactured ceramics.

Acknowledgements

We sincerely appreciate the financial support from the National Natural Science Foundation of China (Nos. 52402084 and 52275310) and the China Postdoctoral Science Foundation (No. 2024M751646).

Availability of data and materials

The data that support the findings of this study are available from the corresponding author upon reasonable request.

Competing interests

The authors have no competing interests to declare that are relevant to the content of this article. The author Rujie He is the Associate Editor of this journal.

References

[1] Teng JC, Li QL, Zhou X, *et al.* Co-enhancement of vat photopolymerized 3D printed silica-based ceramic cores by cristobalite phase transformation and *in-situ* $ZrSiO_4$ formation. *J Alloy Compd* 2025, **1039**: 183029.

[2] Yin J, Geng JY, Wang KL, *et al.* Recent advances in 3D printing and densification of SiC ceramics. *J Inorg Mater* 2025, **40**: 245–255.

[3] Lu XY, Liu G, Lu J. Development of ceramic 3D/4D printing in China. *Addit Manuf Front* 2024, **3**: 200158.

[4] Wang CY, Chen X, Wang ZC, *et al.* A novel mullite anti-gyroid/SiC gyroid ceramic metastructure based on digital light processing 3D printing with enhanced electromagnetic wave absorption and mechanical properties. *J Adv Ceram* 2024, **13**: 1212–1222.

[5] Wang GQ, Shen W, Li YK, *et al.* Improved mechanical performance and forming accuracy of fluorapatite glass-ceramics manufactured using vat photopolymerization with the addition of zirconia. *Addit Manuf* 2023, **74**: 103718.

[6] Zhang H, Yang Y, Hu KH, *et al.* Stereolithography-based additive manufacturing of lightweight and high-strength C_f/SiC ceramics. *Addit Manuf* 2020, **34**: 101199.

[7] Su JJ, Li XY, Liu ZM, *et al.* Mechanical and biological properties of zirconia crowns prepared by digital light processing. *J Am Ceram Soc* 2025, **108**: 20452.

[8] Zhou SX, Zhang SC, Zhang C. Fabrication of ZTA crowns with simultaneously improved isotropy on mechanical property and surface quality by DLP. *Int J Appl Ceram Tec* 2024, **21**: 1593–1615.

[9] Diao Q, Zeng Y, Chen JM. The applications and latest progress of ceramic 3D printing. *Addit Manuf Front* 2024, **3**: 200113.

[10] Zhang KQ, Meng QY, Qu ZL, *et al.* A review of defects in vat photopolymerization additive-manufactured ceramics:

Characterization, control, and challenges. *J Eur Ceram Soc* 2024, **44**: 1361–1384.
[11] Borlaf M, Serra-Capdevila A, Colominas C, *et al*. Development of UV-curable ZrO_2 slurries for additive manufacturing (LCM-DLP) technology. *J Eur Ceram Soc* 2019, **39**: 3797–3803.
[12] Yao YX, Cui HB, Wang WQ, *et al*. High performance dental zirconia ceramics fabricated by vat photopolymerization based on aqueous suspension. *J Eur Ceram Soc* 2024, **44**: 116795.
[13] Jang KJ, Kang JH, Fisher JG, *et al*. Effect of the volume fraction of zirconia suspensions on the microstructure and physical properties of products produced by additive manufacturing. *Dent Mater* 2019, **35**: 97–106.
[14] Sun JX, Binner J, Bai JM. 3D printing of zirconia via digital light processing: Optimization of slurry and debinding process. *J Eur Ceram Soc* 2020, **40**: 5837–5844.
[15] Yared W, Gadow R. Elimination of delamination cracks in ceramics manufactured using LCD stereolithography. *Open Ceram* 2024, **17**: 100531.
[16] Li YF, Chen AN, Su J, *et al*. An overview on ceramic multi-material additive manufacturing: Progress and challenges. *Int J Extreme Manuf* 2025, **7**: 042005.
[17] Li JH, Zhang YZ, Zhao JJ, *et al*. Vat photopolymerization of additively manufactured zirconia ceramic structures from slurries of surface functionalized particles: A critical review. *Surfaces* 2025, **8**: 58.
[18] Reddy PK, Gandhi P, Singh G. Additive manufacturing of yttria-stabilized zirconia using digital light processing: Green density and surface roughness analysis. *Ceram Int* 2024, **50**: 22974–22988.
[19] Zhang LZ, Zeng Y, Yao HH, *et al*. Fabrication and characterization of $ZrO_2(3Y)/Al_2O_3$ micro-ceramic gears with high performance by vat photopolymerization 3D printing. *Ceram Int* 2024, **50**: 5187–5197.
[20] Gong HQ, Wang CY, Wu H, *et al*. Investigating the correlation and composition of organic components in ZrO_2-based slurry on printability improvement and defect suppression of Vat photopolymerization. *Mater Today Commun* 2023, **34**: 105149.
[21] Zhao RS, Yang HB, Liu XT, *et al*. Grain size refinement of additive manufactured Ce-TZP ceramics by coupled two-step pre-sintering and HIP. *J Adv Ceram* 2024, **13**: 621–629.
[22] Zhang KQ, Meng QY, Zhang XQ, *et al*. Roles of solid loading in stereolithographic additive manufacturing of ZrO_2 ceramic. *Int J Refract Met H* 2021, **99**: 105604.
[23] Zhang KQ, He RJ, Ding GJ, *et al*. Digital light processing of 3Y-TZP strengthened ZrO_2 ceramics. *Mat Sci Eng A—Struct* 2020, **774**: 138768.
[24] Hu KH. Study on the process and mechanism of stereolithography-based additive manufacturing for complex ceramic core. Ph.D. Thesis. Beijing (China): Tsinghua University, 2020. (in Chinese)
[25] Liu W, Wu HD, Tian Z, *et al*. 3D printing of dense structural ceramic microcomponents with low cost: Tailoring the sintering kinetics and the microstructure evolution. *J Am Ceram Soc* 2019, **102**: 2257–2262.
[26] Cui GW. *Defects, Diffusion, and Sintering*. Beijing (China): Tsinghua University Press, 1990. (in Chinese)
[27] Huang C, Zheng LY, Tian ZL, *et al*. A warpage-free Si_3N_4 slurry strategy for vat photopolymerization. *J Adv Ceram* 2025, **14**: 9221016.
[28] Saâdaoui M, Khaldoun F, Adrien J, *et al*. X-ray tomography of additive-manufactured zirconia: Processing defects–strength relations. *J Eur Ceram Soc* 2020, **40**: 3200–3207.
[29] Wang JC, Dommati H. Fabrication of zirconia ceramic parts by using solvent-based slurry stereolithography and sintering. *Int J Adv Manuf Tech* 2018, **98**: 1537–1546.
[30] Lian Q, Sui WQ, Wu XQ, *et al*. Additive manufacturing of ZrO_2 ceramic dental bridges by stereolithography. *Rapid Prototyping J* 2018, **24**: 114–119.
[31] Wu XQ, Lian Q, Li DC, *et al*. Influence of boundary masks on dimensions and surface roughness using segmented exposure in ceramic 3D printing. *Ceram Int* 2019, **45**: 3687–3697.
[32] Marsico C, Øilo M, Kutsch J, *et al*. Vat polymerization-printed partially stabilized zirconia: Mechanical properties, reliability and structural defects. *Addit Manuf* 2020, **36**: 101450.
[33] Harrer W, Schwentenwein M, Lube T, *et al*. Fractography of zirconia-specimens made using additive manufacturing (LCM) technology. *J Eur Ceram Soc* 2017, **37**: 4331–4338.
[34] Lian Q, Wu XQ, Li DC, *et al*. Accurate printing of a zirconia molar crown bridge using three-part auxiliary supports and ceramic mask projection stereolithography. *Ceram Int* 2019, **45**: 18814–18822.